

# Microfabricated Electrostatic Actuators for Hard Disk Drives

David A. Horsley, Roberto Horowitz, *Member, IEEE*, and Albert P. Pisano, *Associate Member, IEEE*

**Abstract**—A dual-stage servo system which utilizes a high-bandwidth secondary actuator has been proposed for magnetic hard disk drives. Microfabricated actuators are promising candidates for this secondary actuator, since they offer the benefits of extremely small size and weight and may be batch fabricated for reduced production cost. This paper presents the design of an electrostatic microactuator which produces sufficient output force to move a 1.6-mg picoslider from a conventional disk drive at frequencies above 2 kHz. A linear second-order actuation model is developed and fit to experimental data. The prototype device is shown to have an open-loop resonance frequency of 532 Hz when loaded with the picoslider, and a dc-voltage-to-position gain of  $0.12 \mu\text{m/V}$ . A closed-loop bandwidth of 2.5 kHz is achieved using a simple proportional derivative controller.

**Index Terms**—Disk drive, electrostatic actuation, microfabrication, servo control.

## I. INTRODUCTION

THE areal data density of a magnetic hard disk drive is the product of the linear bit density, which is the number of bits per unit length written along a track, and the track density, which is the number of data tracks per unit length along the radius of the disk. Increases in bit density are achieved by a combination of reduced head/media spacing and increased head sensitivity. Increases in track density, on the other hand, are limited by the ability of the disk drive servo system to position the READ/WRITE elements over the track center. In fact, improvements in linear density are generally the easier to achieve of the two, because they can be implemented by changing the head element, while servo system improvements may require totally redesigning the product.

Despite the fact that servo system improvements may be difficult to implement, there are two major motivations for seeking this goal. The first is that linear densities are presently 10–20 times greater than track densities. While this difference is mainly due to the fact that the width of a recorded bit is proportional to the lithographically defined WRITE head width,

Manuscript received February 6, 1998; revised May 28, 1998. Recommended by Guest Editor W. C. Messner. This work was supported in part by the Defense Advanced Research Projects Agency under Contract DABT 63-95-C-0028.

D. A. Horsley was with the Department of Mechanical Engineering, University of California at Berkeley, Berkeley, CA 94720-1740 USA. He is now with DiCon Fiberoptics, Berkeley, CA 94710 USA.

R. Horowitz is with the Department of Mechanical Engineering, University of California at Berkeley, Berkeley, CA 94720-1740 USA.

A. P. Pisano is with the Electronic Technology Office, Defense Advanced Research Projects Agency, Arlington, VA 22203-1714 USA, on leave from the Department of Mechanical Engineering, University of California, at Berkeley, Berkeley, CA 94720-1740 USA.

Publisher Item Identifier S 1083-4435(98)07146-4.

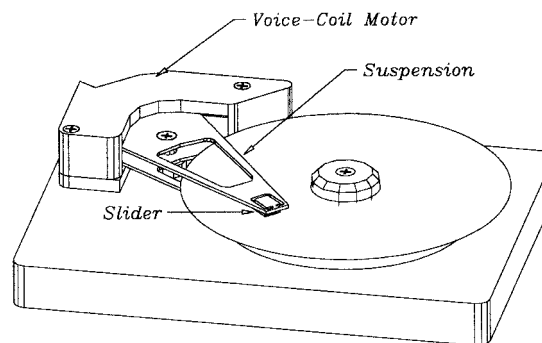


Fig. 1. The basic mechanical components of the conventional servo system.

while the bit length is proportional to the thickness of the insulating film in the head gap, it is clear that major areal density increases can be made by reducing the track width. The second motivation is that the dominating component of data access time is the servo system settling time, which has not kept pace with increases in data rates [1]. As with other areas in disk drive design, incremental improvements in servo performance are constantly being introduced. However, it is becoming clear that the mechanical components of the servo system may be beginning to impair further gains in this area.

## II. SERVO SYSTEM MECHANICS

The basic mechanical components of a conventional disk drive servo system are illustrated in Fig. 1. The READ/WRITE heads are deposited onto the surface of a ceramic slider, which is mounted on the end of a flexible stainless-steel suspension. The suspension is intended to be compliant, in order to allow the slider, which is supported on a hydrodynamic air bearing, to follow the topography of the disk surface. The base of the suspension is attached to a rigid aluminum arm (not shown), which is actuated using an electromagnetic voice-coil motor (VCM). Although the control system has many operating modes, the objective of the track-following controller is to keep the track misregistration (TMR), which is a measure of the deviation of the head position from the track center, within allowable limits.

There are two primary limitations to this system. The first is that nonlinear friction in the pivot bearing which supports the arm results in low-frequency uncertainty in the transfer function from input current to the VCM to output displacement of the slider. The primary effect of this

uncertainty is poor dc tracking accuracy, a problem which is generally corrected through the use of an integrator in the feedback loop, although at the cost of somewhat slower closed-loop response speed. More recently, researchers have presented a more sophisticated scheme utilizing accelerometer-based compensation [2], which should yield improved dc tracking accuracy, albeit at the cost of increased hardware and software complexity. The second limitation of the conventional system is that the sensor (which is the head element itself) and the VCM actuator are not collocated, implying that suspension resonances limit the maximum obtainable closed-loop bandwidth. The first resonance frequency of the 18-mm suspensions commonly used in 3.5-in form-factor drives ranges from 2 to 4 kHz, implying a maximum closed-loop bandwidth of about 800 Hz.

A proposed solution to both the bandwidth and low-frequency tracking accuracy limitations of the conventional system is a two-stage control system which utilizes the VCM in combination with a high-bandwidth secondary actuator. This system has been targeted at future drives which will have areal densities of 10 Gb/in<sup>2</sup> and greater, approximately one order of magnitude greater than the densities in most drives on the market today. The track density required for 10 Gb/in<sup>2</sup> storage has been estimated at 25 000 tracks/in (TPI), corresponding to tracks which are roughly 1- $\mu$ m wide [3]. Although the allowable TMR will depend on the recording head characteristics, an approximate rule of thumb is that the three-sigma value of the TMR is related to the track density  $D_t$  by [4]

$$\text{TMR}_{3\sigma} = \frac{1}{8D_t}. \quad (1)$$

Applying (1), the allowable  $\text{TMR}_{3\sigma}$  at a track density of 25 kTPI is 0.12  $\mu$ m. The fact that single actuator servo systems are currently capable of achieving  $\text{TMR}_{3\sigma} \approx 1 \mu\text{m}$  suggests that the secondary actuator need only have a displacement range of roughly  $\pm 1 \mu\text{m}$ , a range which would span two full trackwidths. The closed-loop bandwidth required to achieve a ten-fold reduction in TMR is not entirely clear. An estimate may be made by noting that the amount of low-frequency attenuation provided in a second-order linear system increases with the square of the closed-loop bandwidth. For this reason, a three-fold increase in bandwidth should provide the necessary reduction in TMR, implying that the secondary actuator should have a bandwidth of 2 kHz or better.

To date, three distinct types of secondary actuators have been proposed. The first type may be classified as an actuated suspension. In this approach, conventional machining and assembly techniques are used to integrate an electromagnetic [5] or piezoelectric actuator into a conventional steel suspension. A clear advantage of these devices is that they rely on proven technologies, but the fact that they must be individually assembled with high precision is expected to result in high unit costs. The second type of actuator may be classified as an actuated head [6]. In this approach, the head elements are deposited onto the surface of a microfabricated actuator which is itself attached to the trailing edge of the slider. This type of actuator is clearly attractive from the standpoint that it requires

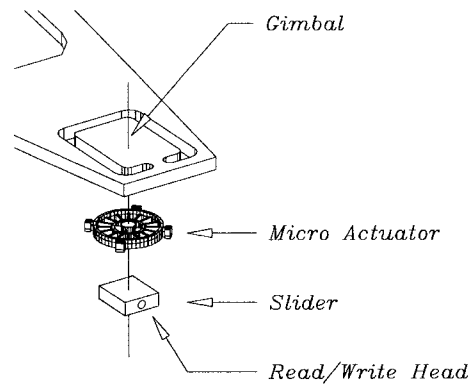


Fig. 2. Exploded view of proposed microactuator/slider assembly.

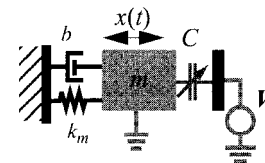


Fig. 3. Simplified schematic of an electrostatic actuator. The fixed stator element is biased at a voltage  $V$  relative to the mobile shuttle, which is grounded.

a minimal amount of moving mass. The obvious drawback is that it adds considerable complexity to the already complicated head fabrication process.

The actuators described in this paper are of a third type, where the actuator is placed between the slider and gimbal of a conventional suspension, as illustrated in Fig. 2. The advantage to this approach is that it relies on a microfabricated actuator to position the picoslider from an existing product. In contrast to the two other approaches described above, these actuators are batch fabricated for low cost, but are not expected to significantly affect either the head or suspension fabrication process. A variety of methods can be used to actuate such a device, including electromagnetic [7], piezoelectric, and electrostatic [3]. Unlike piezoelectric and electromagnetic devices, an electrostatic actuator requires no special materials; rather, the structural material need only be conductive, considerably simplifying the fabrication process. Moreover, electrostatic actuation is naturally compatible with capacitive measurement techniques which allow high-bandwidth high-accuracy displacement measurements.

### III. MICROACTUATOR DYNAMICS

Due to the fact that surface forces, such as friction, are very large relative to inertial forces on microfabricated devices, the moving portions of the actuators described in this paper are supported by a flexural suspension, which prevents contact between moving parts. A simplified schematic for an electrostatic actuator consisting of a fixed stator and a flexurally suspended moving shuttle is shown in Fig. 3. Assuming that the flexure suspension constrains the shuttle motion to a single degree of freedom, the equation describing this motion is that of a simple spring-mass-damper. The displacement  $x(t)$  produced

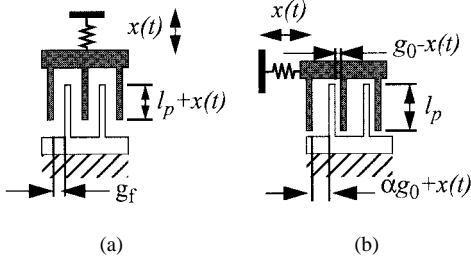


Fig. 4. Capacitive electrode geometries. (a) Interdigitated configuration in which vertical motion of the shuttle causes variations in the electrode overlap. (b) Parallel-plate configuration in which horizontal motion of the shuttle results in variations in the capacitive gap. After [6].

by an electrostatic force  $f(x, V)$  is modeled by

$$(M + m)\ddot{x}(t) + b\dot{x}(t) + k_m x(t) = f(x, V) \quad (2)$$

where  $k_m$  denotes the  $x$ -direction suspension spring constant,  $b$  denotes the damping coefficient, and  $M$  and  $m$  represent the slider and actuator mass, respectively.

#### A. Electrostatic Actuation

The electrostatic force generated by a voltage  $V$  applied between the stator and shuttle is given by

$$f(x, V) = \frac{1}{2} \frac{\partial C(x)}{\partial x} V^2 \quad (3)$$

where  $C(x)$  denotes the capacitance between the shuttle and stator as a function of the actuator displacement  $x$ . The specific expression for  $C(x)$  depends upon the selected electrode configuration. Two common types of electrodes, interdigitated and parallel plate, are illustrated in Fig. 4. As illustrated, these electrode types differ only in the direction of the shuttle motion. Neglecting fringing capacitance, and for sufficiently small shuttle displacements,  $x(t)$ , the capacitance between a pair of interdigitated electrodes of height  $h$  and length  $l_p$ , is given by

$$C_1(x) = \frac{\epsilon_a h (l_p + x(t))}{g_f} \quad (4)$$

while the parallel plate capacitance is given by

$$C_2(x) = \frac{\epsilon_a h l_p}{g_0 - x(t)} \quad (5)$$

where  $\epsilon_a$  denotes the permittivity of air (8.86 pF/m), while  $g_f$  and  $g_0$  represent the nominal interelectrode gap of the interdigitated and parallel-plate configurations, respectively.

Substitution of (4) into (3) yields an expression for the electrostatic force between a pair of interdigitated electrodes:

$$f_1(V) = \frac{1}{2} \frac{\epsilon_a h}{g_f} V^2 \quad (6)$$

while the force generated by each parallel-plate pair is found by substituting (5) into (3)

$$f_2(x, V) = \frac{1}{2} \frac{\epsilon_a h l_p}{(g_0 - x(t))^2} V^2. \quad (7)$$

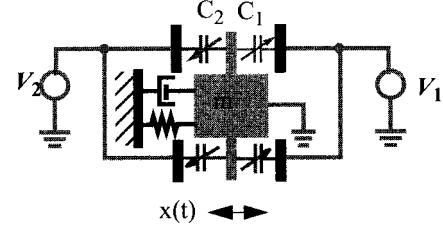


Fig. 5. Electrostatic actuator which is differentially driven using push-pull stator elements.

Note that the interdigitated electrostatic force predicted by (6) is independent of actuator deflection. However, the electrostatic force is greater in the parallel-plate configuration, a fact which may be verified from the ratio of (7) to (6), assuming zero displacement ( $x(t) = 0$ ):

$$\frac{f_2(0, V)}{f_1(V)} = \frac{g_f l_p}{g_0^2}. \quad (8)$$

For equal capacitive gaps ( $g_f = g_0$ ), (8) reveals that the parallel-plate electrostatic force may be an order of magnitude or more greater than the interdigitated force, since the electrode length  $l_p$  is often from 10 to 20 times greater than the capacitive gap  $g_0$ . A drawback of the parallel-plate configuration is that the output force is a function of the displacement. However, because the disk drive application demands a large output force over a narrow range of displacements, the parallel-plate configuration is preferable.

In the configuration which is illustrated in Fig. 4(b), the total parallel-plate electrostatic force on each shuttle electrode is the difference between the force contributed by the left stator electrode and the right stator electrode, which has a larger capacitive gap  $\alpha g_0$

$$f_2(x, V) = \frac{1}{2} \epsilon_a h l_p V^2 \left[ \frac{1}{(g_0 - x(t))^2} - \frac{1}{(\alpha g_0 + x(t))^2} \right]. \quad (9)$$

To minimize the force reduction from the right electrode, the value of  $\alpha$  should be as large as possible. However, increasing  $\alpha$  results in fewer shuttle plates per unit area, reducing the total output force of the actuator. The optimal value for  $\alpha$  depends on the capacitive gap  $g_0$  and the width of each electrode, but is typically from two to three [6].

One approach to linearizing the parallel-plate output force is to use two sets of stator capacitors in a push-pull configuration, so that the net force on the shuttle is the difference between the forces from each stator half, as shown in Fig. 5. A differential input voltage is applied

$$V_1(t) = V_0(t) + v_d(t) \quad (10)$$

$$V_2(t) = V_0(t) - v_d(t). \quad (11)$$

Using this symmetric, differential drive and assuming that the capacitance from the shuttle to each stator is equal, the even terms in the series expansion for the force are eliminated, so that only odd terms remain. In this case, a linear approximation for the electrostatic force is

$$f_T(X(t), V_1(t), V_2(t)) = k_v(V_0)v_d(t) + k_e(V_0)x(t) \quad (12)$$

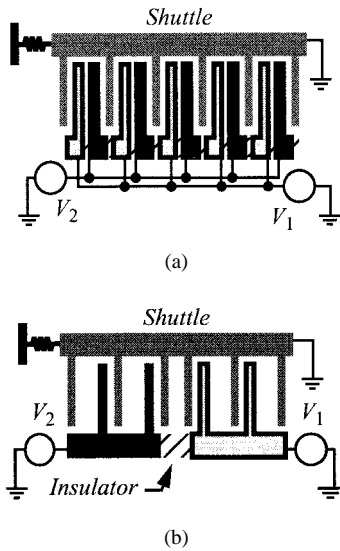


Fig. 6. Parallel-plate electrode configurations. (a) Interlaced push-pull stator electrodes, biased at alternating voltages. (b) Noninterlaced design resulting in reduced interconnect complexity and lower output force.

where  $k_v(V_0)$  and  $k_e(V_0)$  are twice the first-order Taylor-series coefficients of the nonlinear electrostatic force equation from (9) evaluated at the equilibrium point  $(x, V) = (0, V_0)$

$$k_v(V_0) = 2 \left. \frac{\partial F_2(x, V)}{\partial V} \right|_{(0, V_0)} = 2 \frac{\epsilon_a A}{g_0^2} (1 - \alpha^{-2}) V_0 \quad (13)$$

$$k_e(V_0) = 2 \left. \frac{\partial F_2(x, V)}{\partial x} \right|_{(0, V_0)} = 2 \frac{\epsilon_a A}{g_0^3} (1 + \alpha^{-3}) V_0^2 \quad (14)$$

where  $A$  denotes the total capacitive area between the shuttle and each stator half, which is  $Nl_p h$  for an actuator with  $N$  capacitive plates per stator half. An additional advantage to this approach is that the push and pull stator electrodes may be interlaced, so that the value of  $\alpha$  in (9) is infinite. A disadvantage of interlaced electrodes is that they require significantly increased interconnect and electrical isolation complexity, as illustrated in Fig. 6.

### B. Actuator Frequency Response

Substituting the linearized electrostatic force from (12) into the actuator equation of motion given in (2) yields a linear dynamic equation for the actuator displacement

$$(M + m)\ddot{x}(t) + b\dot{x}(t) + k_m x(t) = k_v(V_0)v_d(t) + k_e(V_0)x(t). \quad (15)$$

Note that the last term in (15),  $k_e(V_0)$ , acts to reduce the total spring stiffness of the device, reflecting the tendency of the parallel plates to pull together. In fact, if this electrostatic spring stiffness exceeds the mechanical spring stiffness  $k_m$ , the dynamic system described by (15) will be unstable. The bias voltage at which this occurs is found by setting the two spring terms equal to each other and solving for  $V_0$

$$V_{0, \max} = \sqrt{\frac{k_m(\alpha g_0)^3}{2\epsilon_a A(\alpha^3 + 1)}}. \quad (16)$$

The Laplace transform of (15) is that of a classical second-order system

$$\frac{X(s)}{V_d(s)} = \frac{A_0 \omega_n^2}{s^2 + \frac{\omega_n}{Q}s + \omega_n^2} \quad (17)$$

where  $A_0$ ,  $\omega_n$ , and  $Q$  are the dc gain, natural frequency, and quality factor, respectively. The relationship between these quantities and the coefficients of (15) is given by

$$A_0 = \frac{k_v(V_0)}{k_m - k_e(V_0)} \quad (18)$$

$$\omega_n^2 = \frac{k_m - k_e(V_0)}{m + M} \quad (19)$$

$$Q = \sqrt{\frac{(k_m - k_e(V_0))(m + M)}{b}}. \quad (20)$$

The influence of the softening electrostatic spring term  $k_e(V_0)$  is clearly present in all three of the quantities in (18)–(20). Using this effect, the resonant frequency can be tuned by adjusting the bias voltage, provided that the maximum allowable bias voltage predicted by (16) is not exceeded. This property has been exploited in micromachined inertial instruments, such as gyroscopes, where precise matching of resonance frequencies is required [8].

### C. Selecting the Desired Resonant Frequency

Typical microfabricated actuators exhibit very lightly damped resonances, implying that if the resonant frequency is near the desired servo bandwidth, the settling performance will be poor. One approach is to design the actuator to have an extremely high resonant frequency, so that the actuator dynamics will have negligible effect on the servo system performance. For this approach to succeed, the resonance should be from five to ten times greater than the servo bandwidth. Alternatively, the actuator may be designed to have a resonant frequency which is well within the control bandwidth, requiring active feedback to increase the damping and reduce settling time. The advantage of the latter approach may quickly be seen by noting that the dc gain from input voltage to output displacement listed in (18) may be reexpressed as

$$A_0 = \frac{1}{\omega_n^2} \frac{k_v(V_0)}{(M + m)}. \quad (21)$$

For a fixed mass and bias voltage, (21) states that an actuator which has a resonance frequency which is within the control bandwidth will require 100 times less applied voltage to achieve the same displacement as an actuator with a resonance frequency which is ten times greater. It is tempting to suggest that the resonant frequency be as low as possible, demanding a very compliant flexural suspension. However, because the model in (17) neglects higher order and out-of-plane resonances, this conclusion is erroneous. In order to ensure that these higher order modes can be safely neglected,

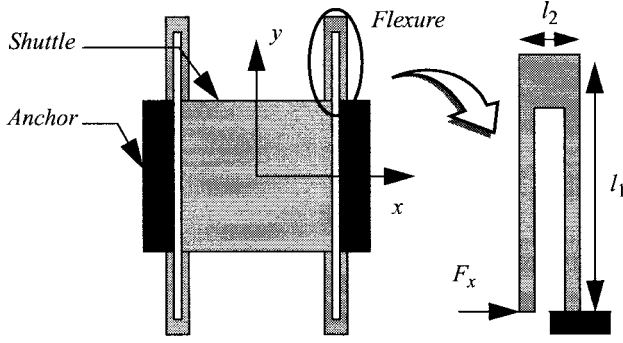


Fig. 7. Folded-beam flexure suspension. Four flexures are symmetrically located at the corners of the moving shuttle. The anchor points also serve as limit stops to prevent the shuttle from overdeflecting.

it is important that the suspension be as stiff as possible in the out-of-plane directions, meaning that the primary resonance frequency  $\omega_n$  should approach the control bandwidth.

#### IV. SUSPENSION DESIGN

One potential suspension design for a translational actuator is shown in Fig. 7. The design, referred to as a folded-beam suspension, consists of four flexures which are symmetrically arranged at the corners of the shuttle. The fixed anchor points, which are biased at the same voltage as the shuttle, also serve as limit stops which constrain the displacement range of the shuttle to prevent the capacitive plates on the shuttle (not shown) from coming into contact with those of the stator. An added advantage of the folded-beam suspension is that it is relatively insensitive to residual stress in the flexures, because the long links of each flexure are free to expand. Insensitivity to residual stress is particularly important in polysilicon micro-machining, as the phosphorous-doped polysilicon is typically deposited with a mean compressive stress. For this reason, if the actuator suspension were composed of fixed-fixed beams, it would be susceptible to buckling, even in the absence of an applied external load.

Bending of the middle link, of length  $l_2$ , may be neglected because this link is much shorter and wider than the other two links, of length  $l_1$ . Additionally, shear stresses are negligible provided that  $l_1$  is approximately ten times greater than the height or width of these two beams. In this case, the approximate suspension spring constant in the  $x$  and  $y$  directions is determined by the bending stiffness of the long links

$$k_m = \frac{24EI_{zz,1}}{l_1^3} \quad (22)$$

$$k_y = \frac{8EI_{zz,1}}{l_2^2 l_1} \quad (23)$$

where  $E$  is the elastic modulus, while  $I_{zz,1}$  is the second moment of area of the long link about the  $z$  axis. For a rectangular cross-sectioned beam of width  $w$  and height  $h$ , this is given by

$$I_{xx,1} = \frac{wh^3}{12}. \quad (24)$$

For a suspension with a height-to-width aspect ratio ( $h/w$ ) which is less than 10:1, the  $z$ -axis spring constant is similar

to the  $x$ -axis spring constant

$$k_z = \frac{24EI_{xx,1}}{l_1^3} \quad (25)$$

where  $I_{xx,1}$  is the second moment of area of the long link about the  $x$  axis, which for a rectangular cross-sectioned beam is

$$I_{xx,1} = \frac{hw^3}{12}. \quad (26)$$

Note that, for this simple case, the ratio of the  $z$ - and  $x$ -axis spring constants is equal to the aspect ratio squared. For beams of greater aspect ratio, shear and torsional stresses may not be neglected, and the suspension spring stiffness is reduced accordingly.

The resonant frequency in the  $y$  direction is related to the primary ( $x$  axis) resonant frequency by the square root of the stiffness ratio

$$\frac{\omega_y}{\omega_n} = \sqrt{\frac{k_y}{k_m}} = \frac{l_1}{\sqrt{3}l_2}. \quad (27)$$

Because the flexures are typically designed so that  $l_1/l_2 > 20$ , the  $y$ -axis resonant frequency is easily a decade higher than the primary resonance. Similarly, the ratio of the  $z$ - and  $x$ -axis resonant frequencies is approximately equal to the height-to-width aspect ratio of the suspension.

An additional concern in the suspension design is the maximum allowable load before the onset of failure. In the case of a ductile material, such as most metals, the failure mode is plastic deformation. On the other hand, brittle materials, such as silicon, fail catastrophically through fracture. Although brittle materials are not generally thought of as reliable choices for engineering materials, the excellent mechanical properties of silicon are well known [9]. Polycrystalline silicon shares many of these same properties [10], but allows additional processing flexibility. The fracture strength of polysilicon is approximately 2 GPa, which is an order of magnitude greater than the yield strength of most metals.

Neglecting combined loading conditions, the maximum normal stress due to bending in each flexure is given by

$$\sigma = \frac{Mc}{I} \quad (28)$$

where  $M$  is the maximum bending moment,  $c$  is the maximum distance from the neutral axis, and  $I$  is the area moment of inertia about the appropriate axis. For a rectangular cross-sectioned beam of width  $w$  and height  $h$ , the resulting stresses for  $x$  and  $y$  loading is

$$\sigma_x = \frac{F_x l_1}{4I_z z/w} \quad (29)$$

$$\sigma_y = \frac{F_y l_2}{4I_z z/w}. \quad (30)$$

Assuming equal loads, the  $y$ -axis bending stress predicted by (30) is an order of magnitude or more lower than the  $x$ -axis stress, because  $l_1/l_2 > 20$ .

## V. MICROFABRICATION TECHNIQUES

Present-day fabrication techniques may be classified as either bulk or surface micromachining. In bulk micromachining, structures are fabricated by selectively etching features into bulk silicon. Surface micromachining, on the other hand, relies on the addition of thin films to the surface of a silicon wafer. These films are then selectively patterned to form the desired structure. The disadvantage of classical polysilicon surface micromachining techniques [11] is that they are limited to film thicknesses of 1–2  $\mu\text{m}$  and can realize height-to-width aspect ratios of no better than 2:1. Novel micromachining methods which rely on highly anisotropic plasma etching have recently been developed which allow aspect ratios of up to 25:1 [12]. One such method uses silicon-on-insulator (SOI) substrates which consist of a 10–100- $\mu\text{m}$  thick layer of silicon bonded onto a full thickness silicon wafer through a thin film of  $\text{SiO}_2$ . High-aspect-ratio structures are patterned into the upper silicon layer using anisotropic plasma etching, and selective removal of the oxide layer releases areas of the structure, leaving them free to move [13]. The advantage to this approach is that the minimum feature size is limited only by the plasma etching process, and capacitive gaps as small as 2  $\mu\text{m}$  may be formed in 0.1-mm-high structures. The disadvantage of this process is that the substrate wafers are relatively expensive, costing over ten times the price of a standard silicon wafer. Additionally, the plasma etching step can be very time consuming, since etch rates are from 1 to 3  $\mu\text{m}/\text{min}$ , and the plasma chamber typically accommodates a single wafer at a time.

An alternative approach is to utilize this same anisotropic silicon etching procedure to pattern a mold into a standard silicon wafer [14]. In this process, known as HexSil, the depth of the mold features determines the height of the finished structure. The completed mold is coated with a sacrificial layer of  $\text{SiO}_2$ , then completely filled with a polysilicon layer which will serve as the structural material. The polysilicon on the wafer surface is then patterned using standard surface micromachining techniques and is released from the mold by selectively removing the oxide layer. A solder bonding process may then be used to assemble the completed actuators onto a target substrate, which serves as the final mounting surface [15]. The advantage of this approach is that the costly plasma etching step is performed only once on a mold wafer which may be reused for multiple fabrication runs. This feature, along with the fact that the process requires no special starting materials, significantly lowers the price of finished parts. Additionally, the solder bonding process allows actuators to be assembled onto an arbitrary substrate, such as a standard CMOS wafer. The disadvantage to this approach is that the minimum capacitive gap is much greater than that achievable in an SOI process, as this gap is increased by twice the 3–4- $\mu\text{m}$  sacrificial layer thickness. A complete discussion of the actuator fabrication process is contained in [16], along with results on rotational microactuators.

### A. HexSil Actuator Layout

The layout of a translational HexSil actuator consisting of  $N = 38$  parallel plates attached to a 1.4 mm  $\times$  1.8 mm

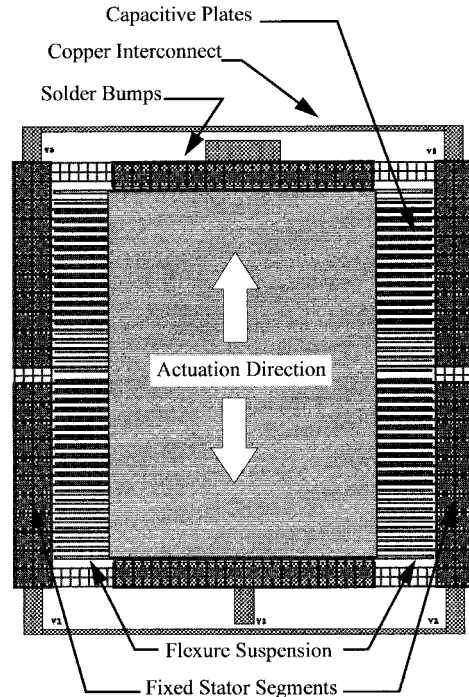


Fig. 8. Translational HexSil actuator consisting of fixed stator segments and a moving central pad which measures 1.4 mm  $\times$  1.8 mm in area.

central pad is shown in Fig. 8. The central pad must be larger than the 1.2 mm  $\times$  1.0 mm picoslider footprint, due to the fact that the present method of bonding the slider onto the actuator does not allow capacitive plates to be placed under the slider. This constraint results in a significant increase in the area occupied by the actuator, and the active capacitive area makes up less than one-third of the total area. New assembly methods which will allow capacitors to be located beneath the slider are currently under development.

An SEM micrograph of a picoslider bonded to a 50- $\mu\text{m}$ -high electrostatic actuator is shown in Fig. 9. Note that, because the actuator is only one-sixth the height of the picoslider and is composed of an open-cell polysilicon grid, the moving mass of the actuator is approximately 90  $\mu\text{g}$ , and the total actuator mass (including the stator elements) is only 110  $\mu\text{g}$ .

## VI. ACTUATOR DESIGN EXAMPLE

### A. Capacitive Area Requirements

The main design criterion is that the actuator have sufficient electrostatic force to position the 1.6-mg picoslider over a range of  $\pm 1 \mu\text{m}$  up to a frequency of 2 kHz. Because the driving voltage will be provided by a charge pump [17], it is assumed that the maximum input voltage is constrained to remain below 80 V. Above the resonant frequency, the actuator payload behaves like a pure inertia, so that the magnitude of the voltage to displacement transfer function asymptotically approaches

$$\left| \frac{X(j\omega)}{V_d(j\omega)} \right|_{\omega > \omega_n} \approx \frac{k_v(V_0)}{(M + m)\omega^2}. \quad (31)$$

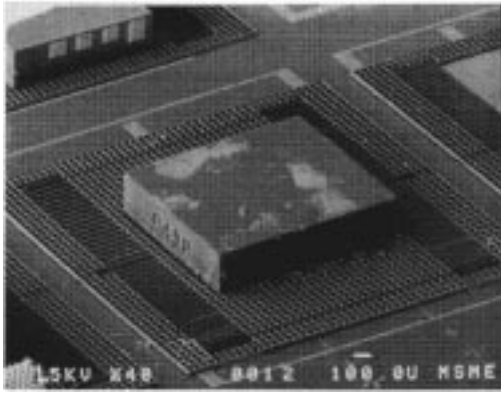


Fig. 9. SEM micrograph of a picoslider bonded to an electrostatic microactuator fabricated using the HexSil process. The picoslider dimensions are 1.2 mm  $\times$  1.0 mm  $\times$  0.3 mm, while the actuator dimensions are 2.2 mm  $\times$  2.0 mm  $\times$  0.05 mm.

As noted earlier, the actuator mass is negligible in comparison to the picoslider mass, so that substitution of numerical values into (31) yields an estimate of the minimum required voltage-to-force gain

$$k_v = (1.6 \text{ mg})(4\pi \times 10^3 \text{ rad/s})(1 \mu\text{m}) = 6.4 \mu\text{N/V}. \quad (32)$$

The current fabrication process has a minimum achievable gap of  $g_0 = 10 \mu\text{m}$ , so that choosing a value of  $\alpha = 2$  (which is close to the optimal value) allows the capacitive area needed to achieve this gain to be calculated from (13), assuming a nominal dc bias voltage of  $V_0 = 40 \text{ V}$

$$A = \frac{g_0^2 k_v (V_0)}{2\epsilon_a V_0 (1 - \alpha^{-2})} = 1.2 \text{ mm}^2. \quad (33)$$

Assuming a maximum actuator height of 100  $\mu\text{m}$  and a capacitive plate length of 0.3 mm, the number of capacitive plates required to achieve this area is  $N = 40$ . Using the same numerical values,  $k_e$  is found to be 38 N/m.

### B. Flexure Dimensions

As the closed-loop bandwidth is expected to be 2 kHz, a nominal ( $x$ -axis) resonant frequency of 1 kHz is suitable. Using the numerical value for  $k_e$  calculated in Section VI-A and noting that the actuator mass  $m$  is negligible in comparison to the picoslider mass  $M$ , the necessary suspension stiffness in the  $x$  direction may be computed from (19):

$$\begin{aligned} k_m &= 38 \text{ N/m} + (2\pi \times 10^3 \text{ rad/s})^2 (1.6 \text{ mg}) \\ &= 101 \text{ N/m}. \end{aligned} \quad (34)$$

For a polysilicon flexure ( $E = 170 \text{ GPa}$ ) of length  $l_1 = 0.3 \text{ mm}$  and height  $h = 0.1 \text{ mm}$ , (18) and (19) may be solved to find that the necessary flexure width is  $w = 4.3 \mu\text{m}$ . Note that these flexure dimensions demand a height-to-width aspect ratio of 25:1, approximately the limit of present-day fabrication techniques. An unfortunate problem is that the flexure stiffness is extremely sensitive to width variations, since the stiffness depends on the width cubed. Thus, if the flexure width varies by  $\pm 0.5 \mu\text{m}$ , the flexure stiffness varies by over 35%.

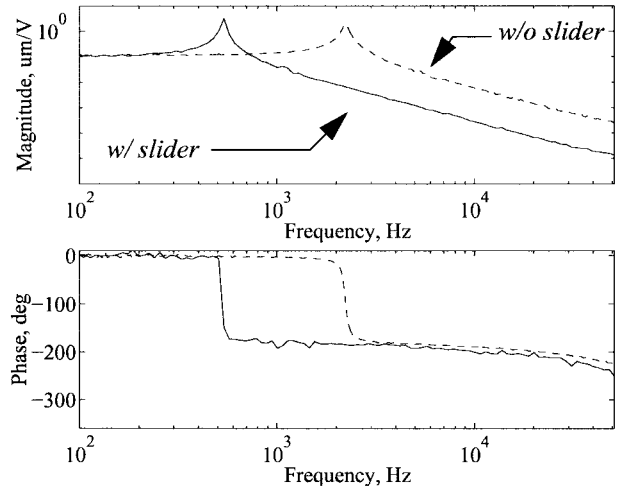


Fig. 10. Measured open-loop voltage to position transfer function, both with and without the picoslider payload.

TABLE I  
MEASURED LINEAR TRANSFER FUNCTION COEFFICIENTS

	$A_0, \mu\text{m/V}$	$f_n, \text{Hz}$	$Q$
w/o slider	$0.117 \pm 0.002$	$2,230 \pm 30$	$34.5 \pm 1$
w/ slider	$0.109 \pm 0.004$	$532 \pm 4$	$110 \pm 10$

## VII. DYNAMIC PERFORMANCE

Electrostatic actuation tests were performed on the actuator shown in Fig. 9, both with and without the 1.6-mg picoslider payload. The input drive voltage was limited to  $\pm 40 \text{ V}$  on top of a 40-V dc bias level. Measurement of the actuator displacement was performed using a laser doppler vibrometer (LDV), which provides up to 2-nm position resolution over a 150-MHz bandwidth. The measured voltage to displacement transfer function, both with and without the picoslider payload, is plotted in Fig. 10. A least-squares fit of the second-order linear transfer function described in (17) was performed for each measured response; the results of the least-squares fits are shown in Table I. Note that the measured actuator performance differed significantly from the designed values for three reasons. First, the actuator height was reduced by a factor of two, from 100 to 50  $\mu\text{m}$ . This difference resulted in a 50% reduction in electrostatic force and suspension stiffness. Secondly, the beam width of the flexure suspension was slightly narrower than designed, resulting in an additional 30% reduction in suspension stiffness. Finally, the capacitive gap was 12  $\mu\text{m}$ , rather than the 10  $\mu\text{m}$  specified in the design, further reducing the electrostatic force by 30%. However, these fabrication flaws are easily corrected and do not represent significant challenges for future devices.

The frequency tuning capabilities of the electrostatic actuator were examined by measuring the dc gain and resonant frequency for multiple bias voltages between 30–50 V. The results of these tests are plotted along with a least-squares fit in Fig. 11. Note that the resonance frequency may be varied

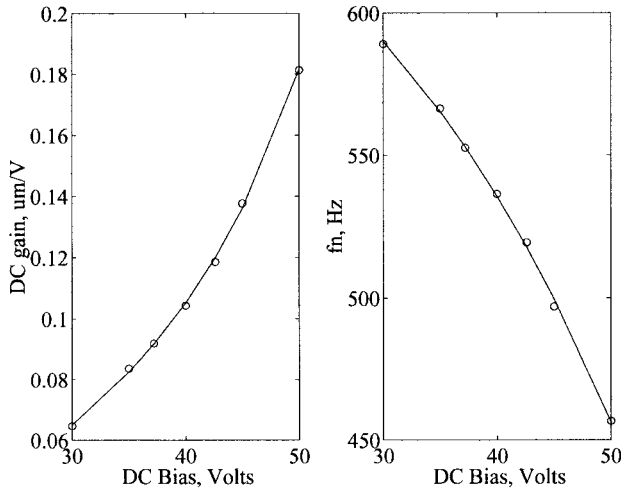


Fig. 11. Measured dc gain and resonant frequency versus dc bias voltage  $V_0$ . Each circle indicates an experimentally measured point, while the solid line indicates a least-squares fit to the data.

TABLE II  
ACTUATOR MODEL PARAMETERS—MEASURED VERSUS THEORETICAL

	$m$ ( $\mu\text{g}$ )	$k_m$ (N/m)	$k_e$ (N/m)	$k_v$ ( $\mu\text{N/V}$ )
Meas.	$97 \pm 10$	$29 \pm 2$	$9.4 \pm 0.6$	$2.0 \pm 1$
Theor.	87	33	10.1	2.2

by approximately  $\pm 10\%$  from the nominal value of 532 Hz. The results of these least-squares fits were used to extract measured values of the parameters of the actuator equation of motion listed in (15). These parameters are listed Table II, along with the values calculated from the theoretical models in Sections III and IV.

### VIII. CLOSED-LOOP CONTROL

There are numerous design techniques which may be used to create a linear controller for a second-order system. Because knowledge of the actuator displacement and velocity corresponds to full-state information, the closed-loop poles may be placed arbitrarily using only position and velocity feedback, or PD control. Under PD control, the closed-loop transfer function from input voltage to output displacement is

$$\frac{X(s)}{V_d(s)} = \frac{A_{0,cl}\omega_{n,cl}^2}{s^2 + \frac{\omega_{n,cl}}{Q_{cl}}s + \omega_{n,cl}^2} \quad (35)$$

where the closed-loop dc gain, natural frequency, and quality factor are related to the open-loop values listed in (17) and the PD controller gains  $k_p$  and  $k_d$  by

$$A_{0,cl} = \frac{A_0}{k_p A_0 + 1} \quad (36)$$

$$\omega_{n,cl} = \omega_n \sqrt{k_p A_0 + 1} \quad (37)$$

$$Q_{cl} = Q \frac{\sqrt{k_p A_0 + 1}}{A_0 \omega_n k_d + 1} \quad (38)$$

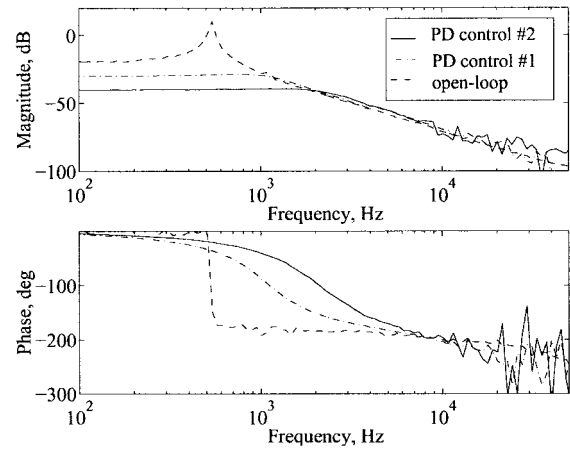


Fig. 12. Measured open- and closed-loop voltage to position transfer function for two sets of PD controller gains. The open-loop transfer function is plotted as a dashed line, while the solid and dash-dot lines represent the closed-loop response.

Note that the only effect of the derivative gain  $k_d$  on the parameters in (36)–(38) is to add damping, since it only appears in the expression for the closed-loop quality factor. The closed-loop gain and natural frequency are, however, related by

$$A_{0,cl}(\omega_{n,cl})^2 = A_0(\omega_n)^2 = \text{constant}. \quad (39)$$

Although slight increases in bandwidth may be obtained at the cost of diminished phase margin, the bandwidth is approximately equal to the natural frequency. Thus, the proportional gain  $k_p$  can be used to trade gain for bandwidth or vice versa. However, as verified by (39), in order to double the closed-loop bandwidth, the closed-loop gain must diminish by a factor of four. Thus, a simple design technique for PD control is to select  $k_p$  to yield either a desired natural frequency or dc gain, then calculate the derivative gain  $k_d$  needed to obtain the desired quality factor. In the case where there are added higher order dynamics, a root locus plot may be used to calculate  $k_d$  for a given  $k_p$ .

#### A. Experimental Results

Two sets of PD controller gains were implemented, one set yielding a closed-loop dc gain of  $0.01 \mu\text{m/V}$  and  $-3$  dB bandwidth of 2.5 kHz, the second a dc gain of  $0.03 \mu\text{m/V}$  and a 1.3-kHz bandwidth. The measured closed-loop voltage to position transfer function for each controller design is shown in Fig. 12. The measured response of the high-bandwidth controller to a  $\pm 5$ -V 500-Hz square wave is shown in Fig. 13. Note that the actuator displacement has settled to within 1% of the final value within 760  $\mu\text{s}$ .

### IX. CONCLUSION

A microfabricated actuator suitable for use as a secondary actuator in a dual-stage disk drive servo system has been presented. The actuator dynamics have been shown to be accurately modeled as a second-order linear system, allowing a simple PD controller to be used for closed-loop positioning.

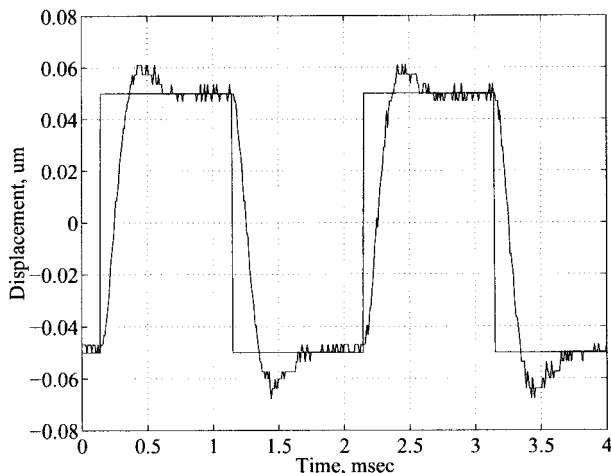


Fig. 13. Closed-loop response to a  $\pm 5$ -V 500-Hz square-wave input, using the high-bandwidth PD controller. The reference waveform has been generated by multiplying the input voltage by the closed-loop dc gain.

A closed-loop bandwidth of 2.5 kHz was achieved, yielding a measured 1% settling time of 760  $\mu$ s. Although the prototype devices have a smaller dc gain than originally specified, simply doubling the fabricated height of future devices will correct this limitation.

#### ACKNOWLEDGMENT

The authors thank S. Williams of Quantum Corporation for providing picosliders, M. Cohn and A. Singh for their work on solder-bump assembly of microstructures, as well as J. Bustillo and the staff of the Berkeley Microfabrication Laboratory for their continued assistance.

#### REFERENCES

- [1] N. Schirle, "Key mechanical technologies for hard disk drives," presented at the Int. Conf. Micromechatronics for Information and Precision Equipment, Tokyo, Japan, July 1997, Paper MR-K1.
- [2] J. Ishikawa and M. Tomizuka, "Pivot friction compensation using an accelerometer and a disturbance observer for hard disk drives," in *Proc. ASME Conf. Information Storage and Processing Systems*, 1997, vol. 3, pp. 83–89.
- [3] L.-S. Fan, H. H. Ottesen, T. C. Reiley, and R. W. Wood, "Magnetic recording-head positioning at very high track densities using a microactuator-based, two-stage servo system," *IEEE Trans. Ind. Electron.*, vol. 42, pp. 222–233, June 1995.
- [4] C. D. Mee and E. D. Daniel, *Magnetic Storage Handbook*, 2nd ed. New York: McGraw-Hill, 1996.
- [5] S. Koganezawa, K. Takaishi, Y. Mizoshita, Y. Uematsu, and T. Yamada, "Development of integrated piggyback milli-actuator for high-density magnetic recording," presented at the Int. Conf. Micromechatronics for Information and Precision Equipment, Tokyo, Japan, July 1997, Paper MR-08.
- [6] T. Imamura, T. Koshikawa, and M. Katayama, "Transverse mode electrostatic microactuator for MEMS-based HDD slider," in *Proc. 9th Int. Workshop Micro Electro Mechanical Systems (MEMS '96)*, San Diego, CA, Feb. 1996, pp. 216–221.

- [7] W. Tang, V. Temesvary, R. Miller, A. Desai, Y. C. Tai, and D. K. Miu, "Silicon micromachined electromagnetic microactuators for rigid disk drives," *IEEE Trans. Magn.*, vol. 31, pp. 2964–2966, Nov. 1995.
- [8] W. A. Clark, R. T. Howe, and R. Horowitz, "Surface micromachined z-axis vibratory rate gyroscope," in *Proc. 1996 Solid-State Sensor and Actuator Workshop*, Hilton Head, SC, June 1996, pp. 283–287.
- [9] K. Petersen, "Silicon as a mechanical material," *Proc. IEEE*, vol. 70, pp. 420–457, May 1982.
- [10] W. N. Sharpe, Jr., B. Yuan, R. Vaidyanathan, and R. L. Edwards, "Measurements of young's modulus, Poisson's ratio, and tensile strength of polysilicon," in *Proc. 10th Int. Workshop Micro Electro Mechanical Systems (MEMS '97)*, Nagoya, Japan, Feb. 1997, pp. 424–429.
- [11] R. T. Howe, "Surface micromachining for microsensors and microactuators," *J. Vac. Sci. Technol. B, Microelectron. Process. Phenom.* vol. 6, no. 6, pp. 1809–1813, Nov./Dec. 1988.
- [12] J. K. Bhardwaj, H. Ashraf, and A. McQuarrie, "Dry silicon etching for MEMS," presented at the Symp. Microstructures and Microfabricated Systems, Electrochemical Society Annu. Meeting, Montreal, P.Q., Canada, May 1997.
- [13] T. J. Brosnihan, J. M. Bustillo, A. P. Pisano, and R. T. Howe, "Embedded interconnect and electrical isolation for high-aspect-ratio, SOI inertial instruments," in *Proc. 1997 Int. Conf. Solid-State Sensors and Actuators (Transducers '97)*, Chicago, IL, June 1997, pp. 637–640.
- [14] C. G. Keller and M. Ferrari, "Milli-scale polysilicon structures," in *Proc. 1994 Solid-State Sensor and Actuator Workshop*, Hilton Head, SC, June 1994, pp. 132–137.
- [15] M. B. Cohn, Y. Liang, R. T. Howe, and A. P. Pisano, "Wafer-to-wafer transfer of microstructures for vacuum packaging," in *Proc. 1996 Solid-State Sensor and Actuator Workshop*, Hilton Head, SC, June 1996, pp. 32–35.
- [16] D. A. Horsley, A. Singh, A. P. Pisano, and R. Horowitz, "Angular micropositioner for disk drives," in *Proc. 10th Int. Workshop Micro Electro Mechanical Systems (MEMS '97)*, Nagoya, Japan, Feb. 1997, pp. 454–459.
- [17] P. Favrat, L. Paratte, H. Ballan, M. Declercq, and N. F. deRoosij, "A 1.5 V supplied, CMOS ASIC for the actuation of an electrostatic micromotor," in *Proc. 9th Int. Workshop Micro Electro Mechanical Systems (MEMS '96)*, San Diego, CA, Feb. 1996, pp. 25–31.

**David A. Horsley**, for a photograph and biography, see this issue, p. 165.

**Roberto Horowitz** (M'89), for a photograph and biography, see this issue, p. 155.



**Albert P. Pisano** (A'84) received the B.S. degree in 1976, the M.S. and M.Phil. degrees in 1978, and the Ph.D. degree in 1981 from Columbia University, New York, NY.

He was a Member of the Research Staff at Xerox Corporation from 1981 to 1983, prior to joining the Department of Mechanical Engineering, University of California at Berkeley, in 1983. He is currently the MEMS Program Manager with the Electronic Technology Office, Defense Advanced Research Projects Agency, Arlington, VA, on leave from the University of California at Berkeley, where he serves as a Co-Director of the Berkeley Sensor and Actuator Center, an NSF/Industry/University Research Cooperative. He conducts research in the areas of design, optimization, and fabrication of microactuators, microbiological devices, micro inertial instruments, and micro test devices (for friction and impact measurements), all in the size range from 100 to 1000  $\mu$ m.